The Failiur Ananlysis of Nb-Microalloyed δ-Trip Steel

S. Gholami Shiri[1,2], Y. Palizdar[3], S. A. Jenabali Jahromi[*1] and E. F. De Monlevade[4]

* *s.a.jenabalijahromi@gmail.com*

Received: February 2018 Accepted: June 2018

[1] Department of Materials Science and Engineering, School of Engineering, Shiraz University, Shiraz, Iran.

[2] Damavand Petrochemical Company, Phase 2, Pars Special Economic Energy Zone, Boshehr, Iran.

[3] Nanotechnology and Advanced Materials Department, Materials and Energy Research Center, Karaj, Iran.

[4] Department of Metallurgical and Materials Engineering, Polytechnic School, University of São Paulo, São Paulo, Brazil.

DOI: 10.22068/ijmse.15.3.32

Abstract: *The relation between microstructure and the fracture mechanisms of δ-TRIP steel with different Nb-content has been investigated using complementary methods of light microscopy, SEM, EDS, EBSD, X-ray phase analysis and tensile test. The results revealed a close dependency between the presences of constitutive phases i.e. ferrite, bainite, retained austenite and martensite and the mode and characteristics of fracture. All samples revealed almost different fractography pattern which could be associated to the effect of Nb microalloying element. The different fractography patterns were consisted of dimple rupture, riverside and Wallner lines pattern. The proportion of the cleavage fracture in comparison of dimple rapture increased by increasing the Nb-content due to the increase of primary martensite in the microstructure.*

Keywords: *δ-TRIP steel, High Al steel, Fracture mode, Fractography, Nb-microalloyed.*

1. INTRODUCTION

The success of TRIP-assisted multiphase steels comes from simultaneous combination of high strength and superior ductility which are the advantages of the multiphase microstructure and appearance of TRIP effect in this type of steels [1, 2]. During the deformation, the continuous generation of the fresh dislocations in the adjacent ferrite occurs as a consequence of the volume expansion of TRIP phenomena [3]. This result in the outstanding plastic deformation and the work hardening of ferritic phases [4]. The presence of Si or Al in the chemical composition of these steel is essential to obtain suitable fraction of retained austenite due to effectively delay the precipitation of carbide during heat treatment process [2, 3]. In a recent work by the authors [5] it was shown that in the high-Al TRIP-assisted (δ-TRIP) steel, the δ-ferrite is present as a major phase in all solid states which contributes to excellent tensile properties. The results also revealed the unexpected decrease of tensile strength by addition of Nb as a microalloying elements.

δ-TRIP steels have been taken under study from different aspects such as microstructure [6, 1, 2], transformation features [6, 2], optimizing heat treatment parameters and composition [4, 7, 8], hot deformation behavior [9, 10, 11] and mechanical properties [11, 12]. However, studies on the fracture feature of TRIP steels have been limited to few attempts by G. Lacroix et al. [13] and H.S. Wang [14]. The fracture feature or failure patterns of TRIP steels could be survey by fundamentally investigation of the phase transformation during the tensile test as well as fracture surface. Fracture is, often, the culmination of continued deformation processes. Therefore, fracture surface may retain signature of the deformation processes that a material was subjected to. The change in the contribution of the size, morphology and amount of retained austenite with increase in Nb-content led to dramatic change in the mode and characteristics of fracture. The objective of the study is to investigate the effect of Nb in governing mechanical properties and fracture behavior in hot-rolled Fe-0.43C-1.35Mn-3.9Al TRIP steels.

2. EXPERIMENTAL

The chemical compositions of the studied alloys which consist of Nb-free reference material and two Nb microalloyed steels are

[DOI: 10.22068/ijmse.15.3.32]

Table 1. The chemical compositions (wt. %) of the investigated specimens.

	C	Mn	Si	Al	Cr	Mo	Ni	Cu	Nb	S	P
Sample A	0.43	1.33	0.86	3.91	0.02	0.07	0.1	0.02	-	0.08	0.003
Sample B	0.43	1.35	0.86	3.87	0.014	0.07	0.1	0.04	0.03	0.08	0.003
Sample C	0.44	1.31	0.87	3.97	0.02	0.06	0.1	0.014	0.07	0.09	0.003

listed in Table 1. The alloys were prepared as ingots of 60×70×240 mm dimensions using a vacuum induction furnace (VIM). The Electro Slag Refining (ESR) process was performed on the ingots to reduce the sulfur and phosphor content. The ingots were reheated for 10 min at 1200 °C for the hot rolling process to make the 10 mm strip at the finishing temperature of about 900 °C followed by the air cooling to room temperature.

In order to obtain a TRIP-assisted steel, a two-step heat treatment was carried out. To establish the appropriate heat treatment schedule, the intercritical temperature range was determined by the means of Differential Thermal Analysis (DTA). The DTA results of the investigated steels are presented in Figure 1. Based on aforementioned analysis, the austenite and ferrite coexist between 734 °C and 845 °C. Therefore, the samples were intercritically annealed (IA) in the electric furnace at 820 °C, followed by fast quenching into the salt bath at 420 and held for 120s and finally air cooled to the room temperature. The Isothermal Bainite Transformation (IBT) temperature was selected just above the martensite-start temperature (M_s) which was calculated empirically using the following equation [8]:

$$MS(°C)=539-423W_C-30.4W_{Mn}-17.7W_{Ni}-12.1W_{Cr}-11W_{Si}-7W_{Mo}+30W_{Al} \quad (1)$$

where W_C, W_{Mn}, W_{Ni}, W_{Cr}, W_{Mo} and W_{Al} are the mass contents of the elements in the austenite.

For the microstructural characterization, the specimens were cut along the longitudinal and vertical axis and the obtained sections were carefully prepared by applying standard metallographic techniques consisting of grinding with emery up to 3000-grit abrasive paper followed by polishing. The optical microscopy (OM) was carried out on the samples etched with the tint-etchant technique based on the metabisulfite salt solution (mixed of 1% aqueous solution of sodium metabisulfite and 4% picral that were mixed in a 1:1 ratio) to visualize the different phases in the complex microstructure of the δ-TRIP [15]. The etched samples were also examined by the VEGA/TESCAN scanning electron microscope (SEM) equipped with an energy dispersive X-ray spectroscopy (EDS) as well as electron back-scattered diffraction (EBSD). The SEM and OM micrographs were used to determine the distribution, size (width), morphology and the volume fraction (with the aid of image analyzer software) of each phase. X-ray diffraction (XRD) technique, which was carried out in a PHILIPS X'Pert diffractometer using the CoKα radiation (λ=1.78897A˚), was also employed for the details phase analysis. The volume fraction of the austenite was determined by the X-ray diffraction (XRD) using a direct comparison method, involving the use of integrated intensities of (200)α and (211)α peaks and those of (220)γ and (311)γ peaks by the follow equation [5, 8, 16]:

$$V_A=1.4I_\gamma/(I_\delta+1.4I_\gamma) \quad (2)$$

where I_γ is the integrated intensity of austenite and I_δ is the integrated intensity of α-phase.

The carbon content of the austenite was also determined by the XRD results, using a direct comparison method and from the lattice parameter (a_0) using the combined equations proposed by Ruhl and Cohen and the empirical equation by Dyson and Holmes respectively [8].

[DOI: 10.22068/ijmse.15.3.32]

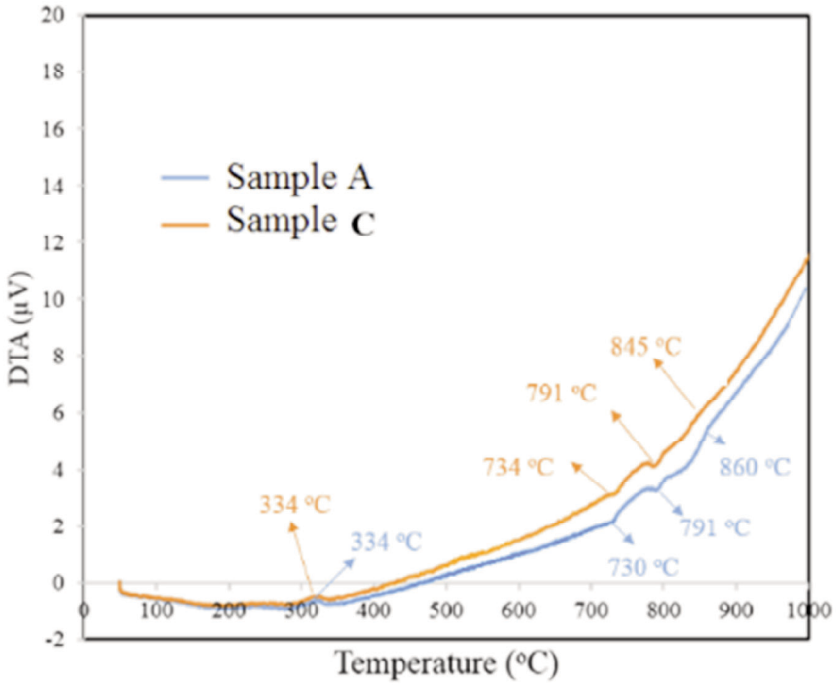

Fig. 1. DTA curve for as rolled sample A and C.

The tensile tests were carried out parallel to the rolling direction to determine the tensile properties of the specimens. The tensile properties of each steel was evaluated using three rounded tensile specimens cut from the same steel with the gage length of 30 mm, 6 mm in diameter (according to the ASTM E8 standard) and crosshead speed of 3 $mm.min^{-1}$ in an MTS universal testing machine with a load range of 50000 N. The fractured surfaces of tensile tested specimens have been examined using the scanning electron microscope.

3. RESULTS AND DISCUSSION

The details of as-cast microstructure as well as the evolution of the microstructure during the hot rolling process can be found elsewhere [5], however, the obtained results have been summaries in table 2. Fig. 2 (a) shows the OM image of the sample A as the Fig. 2 (b-d) shows the SEM images of $A_{420/120}$, $B_{420/120}$ and $C_{420/120}$ respectively. In Fig. 2 (a), the bands of the coarse ferrite in all the samples can be associated with the persistence of the δ-ferrite at the hot rolling process. The δ-ferrite and α-ferrite can be distinguished simply by identifying the former as having been retained from the solidification and has persisted through the hot-deformation, whereas α is the result of transformation from the austenite. In Fig. 2 (b-d), multi-phase structure of δ-ferrite, α-ferrite, ferritic bainite and retain austenite/martensite (A/M) has been labeled in these micrographs. Fig. 2 (b) shows a typical sheaf structure constituted of parallel platelets of bainitic ferrite, separated by films of retained austenite, that are spread in the continuous matrix of δ-ferrite. As clearly can be seen in Fig. 2 (b, c and d), the amount of sheaf bainite decrease sharply by addition of Nb and the morphology of A/M change from sheaf structure to blocky. K. Hausmann and et al [6] declared that the amount of isothermal bainite is less for Nb microalloyed steels and a change in morphology of the bainitic matrix from lath-like to globular was observed as a result of grain refinement. The A/M fractions measured by a point counting method from microstructure images are about 12, 14 and 15±

[DOI: 10.22068/ijmse.15.3.32]

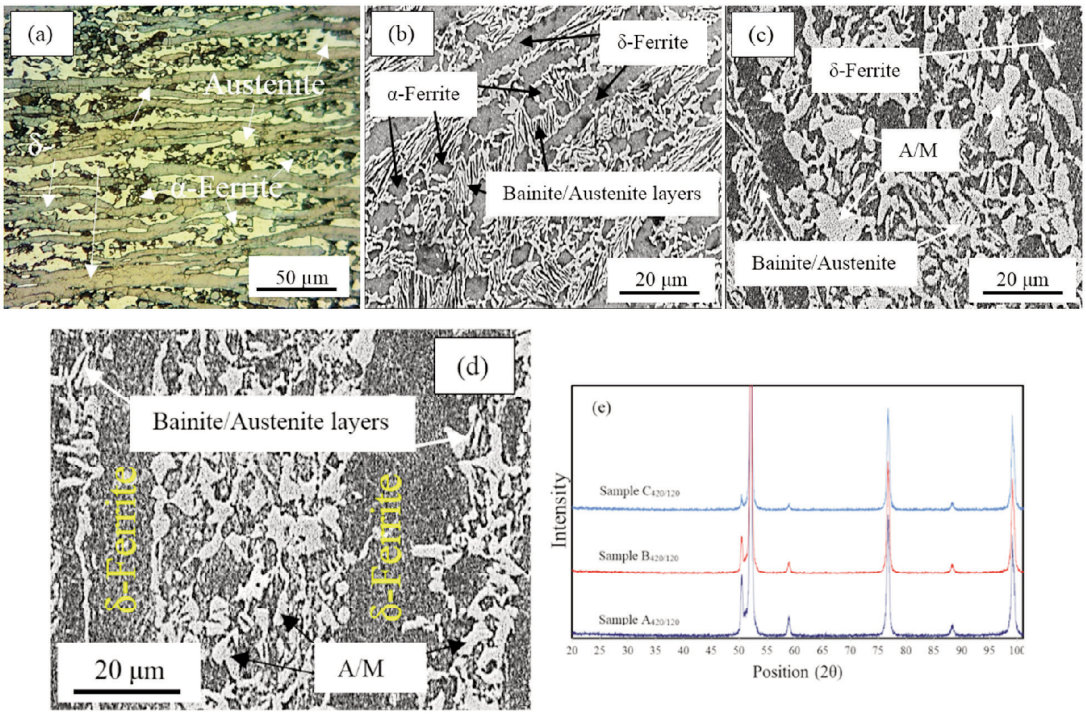

Fig. 2. The OM image of sample Aas-rolled and the SEM image of the sample (a) A420/120, (b) B420/120, (c) C420/120 and (d) XRD pattern of these samples.

1.4 vol.% . On the other hand, according to the XRD results, the austenite fractions are 11, 4.7 and 3.2 at the carbon concentration of 1.32, 0.98, 0.91 wt. % for sample $A_{420/120}$, $B_{420/120}$ and $C_{420/120}$ respectively. The difference in the calculated austenite volume fraction in SEM and XRD technique could be due to the transformation of austenite to martensite during cooling to ambient temperature. It is well-known that the high carbon contents in retained austenite caused by the rejection of carbon atoms from adjacent grains during IBT [8, 6]. The carbon atoms could diffuse more easily from surrounding grains to sheaf type retained austenite through large interface but short diffusion path. The difference in carbon content could affect the Ms and subsequently the stability of austenite. Thus, the untransformed austenite has a higher carbon content compared to the bulk of the alloy. Consequently, the Ms temperature of the untransformed austenite is decreased. The M_s temperature of the untransformed austenite was measured to be -5, +93 and +115 ℃ for sample $A_{420/120}$, $B_{420/120}$ and $C_{420/120}$ respectively. This demonstrates that the susceptibility of austenite to martensite transformation in the samples $B_{420/120}$ and $C_{420/120}$ is higher and the austenite phase easily transformed to the martensite during cooling to room temperature as has been proved later by comparing the XRD and SEM results.

In order to investigate the different phases after the heat treatment process, the EBSD phase maps were obtained as shown in Fig. 3. The red and green colors represent the ferrite (bcc) and austenite (fcc) phases, respectively. As the Nb content increased (Fig. 3(c)), the volume fraction of black region which were unidentified phases, due to low confidence index (less than 0.1), was also increased in EBSD phase maps. It is believed that these unidentified regions could be assumed as martensite, which has low confidence index due to pattern damaged caused by transformation of austenite to martensite during cooling to room temperature. As can be seen in these pictures, there are a few amount of the austenite which transform to martensite in sample A with sheave structure, while austenite in the sample C transform to martensite during

[DOI: 10.22068/ijmse.15.3.32]

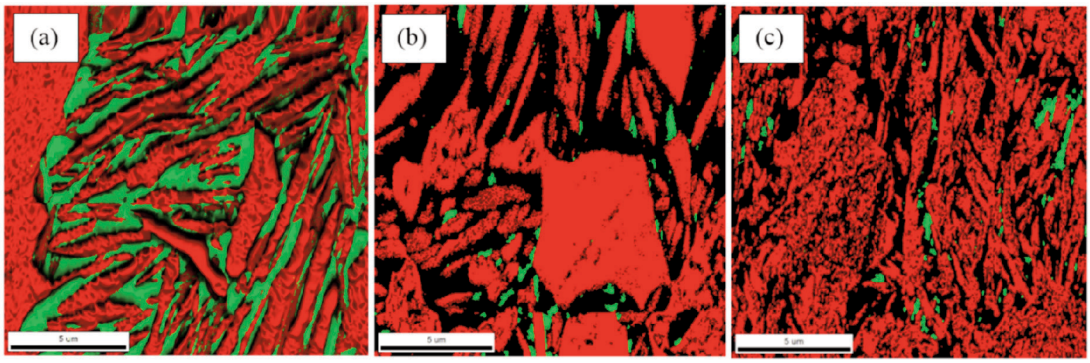

Fig. 3. EBSD phase maps of the samples (a) $A_{420/120}$ before deformation, (b) $A_{420/120}$ after deformation in gage length area and (c) $C_{420/120}$.

cooling to ambient temperature. Comparing Fig. 3(a) and (b) confirms the transformation of austenite to martensite during deformation and occurrence of TRIP phenomena.

4. MECHANICAL PROPERTIES

The performance of the selected samples under the tensile test was investigated to reveal the mechanical properties of the samples. The tensile properties results obtained from samples A, B and C in the as-rolled condition and heat treated are summarized in Table 2. Nonetheless, the results reveled an unexpected decrease in the tensile strength of the specimens by addition of Nb. It should be noted that the sample $A_{420/120}$ illustrates the best combination of strength and ductility which seems to be the consequence of relatively high volume fraction of retained austenite (11 vol.%) with high carbon content (1.32 wt.%). This could result in high mechanical stability of the retained austenite and thus more gradual martensitic transformation during the deformation. The unexpected decrease of the tensile strength with increasing Nb content could be explained as follow:

The presence of high Nb with higher atomic radius in the austenite generated the internal strain and this could create the nucleation site for transformation of martensite and thus the reduction of the stability of austenite [8, 11]. On the other hand, the EDS analysis of the sample $C_{420/120}$ (Fig. 4) revealed the partitioning of Nb in the austenite grains especially in the vicinity of δ-ferrite interface in Nb microalloyed samples. The presence of the Nb as well as C in the austenite may lead to the buildup of NbC in these regions. K. Hausmann and et.al. [6] based on the TEM investigation, showed the presence of the fine and coarse NbC particles in the range of 5.7 to 6.7 nm and 73 to 89 nm respectively in the three grades of TRIP –assisted steel in the 0.025, 0.045

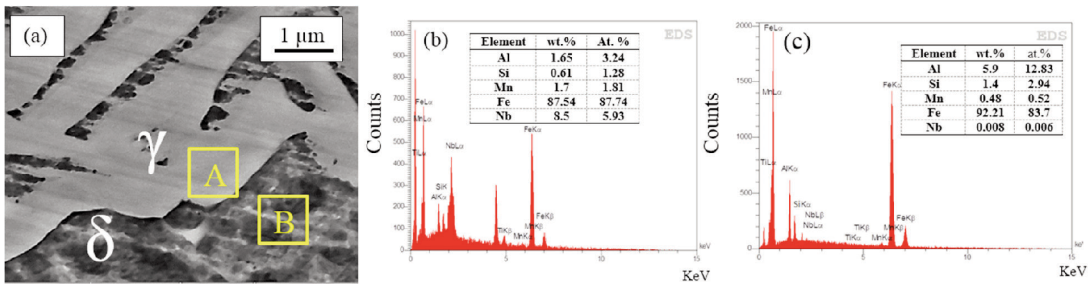

Fig. 4. (a) The SEM images of sample $C_{420/120}$, (b) The EDS analysis near the interface of δ/γ in γ (Point A) and, (c) EDS analysis of δ-ferrite (Point B)

[DOI: 10.22068/ijmse.15.3.32]

Table 2. Summary of phase constituent and mechanical properties.

Samples	%γ	%C in γ	Chemical composition of γ**	M_S(°C)***	YS(MPa)	UTS (MPa)	UE%	TE%
$A_{as\text{-}rolled}$	32*	0.79	1.69Mn-0.62Si-1.8Al	200	840	1144	23.2	25.1
$B_{as\text{-}rolled}$	25*	0.83	1.7Mn- .64Si-1.83Al	184.8	705	950	23.6	26.3
$C_{as\text{-}rolled}$	22*	0.88	1.70Mn- 0.61Si-1.73Al	161	710	917	26	28.1
$A_{420/120}$	11	1.32	1.78Mn- .57Si-1.53Al	-5	851	1167	25	31
$B_{420/120}$	4.7	0.98	1.76Mn- 0.51Si-1.6Al	+93	707	951	22	29.3
$C_{420/120}$	3.2	0.91	1.75Mn- 0.53Si-1.55Al	+115	703	926	17	28.2

* In the As-rolled specimens, the amount of A/M has been reported.
**The results were obtained by EDS analysis.
***The M_s Temperature were calculated by equation 1.

and 0.90 wt.% Nb microalloyed. Thus this partitioning of Nb could result in one of the following situations; first, the precipitation of large amount of Nb(C,N) which consumes the carbon in the austenite and thus decrease the stability of austenite. Second, the precipitation of large amount of Nb(C,N) strengthen the austenite in the vicinity of δ-ferrite grains and thus the two phase with different strength are situated in close proximity to each other. Therefore this generate the weak are of the specimen and crack can be initiate from this region.

Furthermore, the morphology of bainite and austenite change from sheave structure to blocky by increasing the amount of Nb in the chemical composition as illustrated in Fig. 2 (b-d). It has been proved that the mechanical stability of the blocky type austenite was lower than that of the sheaf type one [5, 6, 11, 12]; which means that the blocky type retained austenite would be easily transformed into the martensite. It is considered that many defects existing in the blocky type austenite could work as the nucleation site of martensite transformation. In contrast, the high carbon contents, bainite and transformed martensite would increase the resistance to shear transformation, resulting in the inhibition of transformation of austenite to martensite [12, 15]. It has been proven that the final mechanical properties depends upon the kinetics of the austenite into martensite transformation, which is strictly connected with the austenite phase stability that is mostly dependent on the carbon concentration of the austenite [16]. According to the XRD results, the carbon content of the film type austenite was higher than those of blocky type austenite. The EBSD images revealed the presence of martensite even before deformation in the sample $C_{420/120}$, while there was no considerable presence of martensite in the microstructure of $A_{420/120}$. Therefore, these regions have more potential for crack initiation. . It is surprising that the freshly produced high-carbon martensite does not impair the ductility even carbon embrittles martensite [8]. It has been shown that the tendency of the martensite to initiate a crack in a mixed microstructure of the austenite and martensite depends on its absolute size. In TRIP-assisted steels, it is difficult to transfer load onto the martensite when the composite mixture is strained. When the austenite grain size is coarse it's however prone to form long plates of martensite, which are potent for crack [16].

5. FRACTOGRAPHY

The fracture surface analysis procedure entailed the examination of a metallographic section containing a profile of the fracture surface. Using this technique, it is possible to obtain important information about the fracture path. For example, by comparing the path of the fracture with the metallographic grain structure, it was possible to determine whether the failure has a transcrystalline or intercrystalliue nature. Fig. 5(a-d) illustrates the SEM macrographs of the fractured surface of the samples A420/120 and C420/120 while the Fig. 5(e) illustrates the OM image of the specimen Cas-rolled at 1mm distance of the fractured surface. In the sample

[DOI: 10.22068/ijmse.15.3.32]

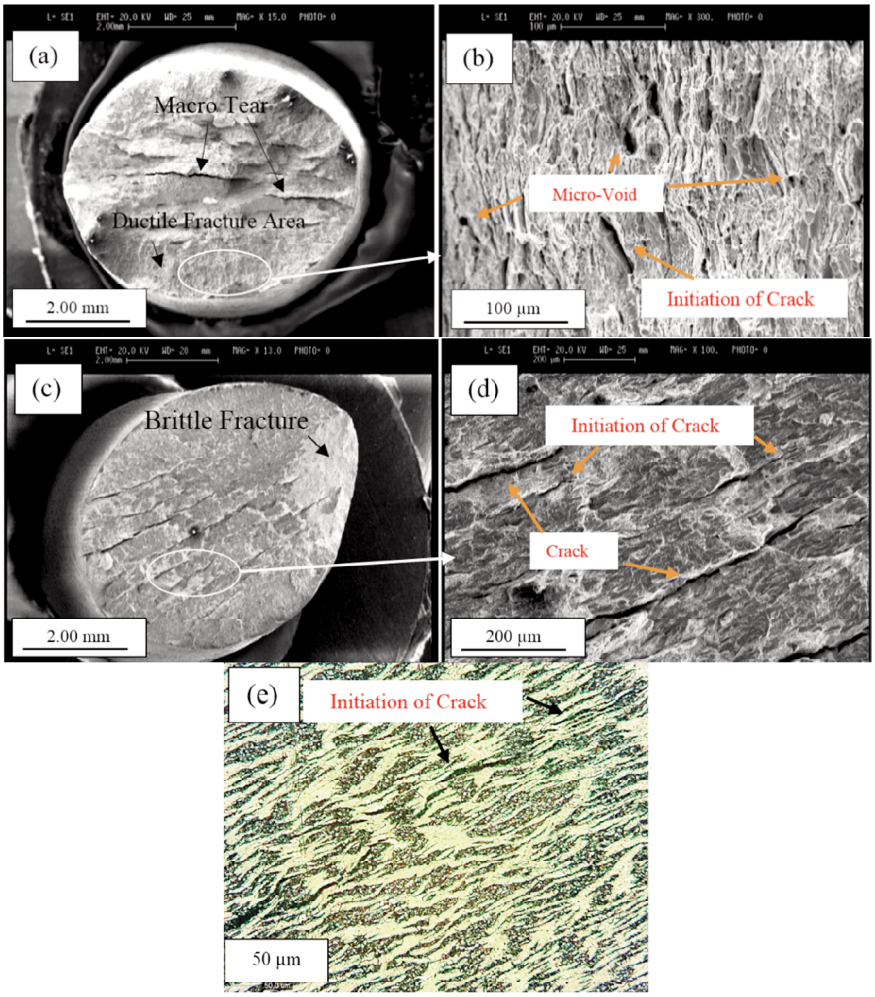

Fig. 5. a) and b) the SEM macrographs of fractured surface of the samples $A_{420/120}$ c) and d) sample $C_{420/120}$ in different magnification and e) the OM image of the specimen Cas-rolled at 1mm below the fractured surface.

$A_{420/120}$ (Fig. 5(a)), the fractured surfaces consisting of rough splintered surface around the tensile specimen which is the indication of ductile the fracture as well as the macro tears in the middle of the samples. It has been observed that the fractured surface is exactly normal to the tensile load direction. Fig. 5(b) clearly illustrates the nucleation of the microvoid and subsequently microvoid coalescence which is observed in the most metallic alloys and many engineering plastics, followed by their growth and eventual coalescence. In this sample, the growth mechanisms have been identified by plastic flow of the matrix that surrounds the nucleation site. The final step of microvoid coalescence that leads to final failure involves the coalescence of countless microvoids into large cracks. Often, this process occurs by the necking down of material ligaments located between the adjacent microvoids, thereby leading to the impingement of the adjacent microvoids [17]. In other circumstances in sample $C_{420/120}$, the fracture surface has a deviation of 30 degrees from the load direction. The fractured surfaces consisting of shiny angular facets in almost the entire fractured area and the smooth featureless area at the corner, specifies the final rapture place of tensile specimen and macro tears exist in all part of the samples. The images are apt descriptions of the fracture texture.

Fig. 5(e) reveals the transcrystalline crack propagation and intercrystalline crack growth at the sample Cas-rolled. The initiation of the crack from the interface of austenite and ferrite can be

[DOI: 10.22068/ijmse.15.3.32]

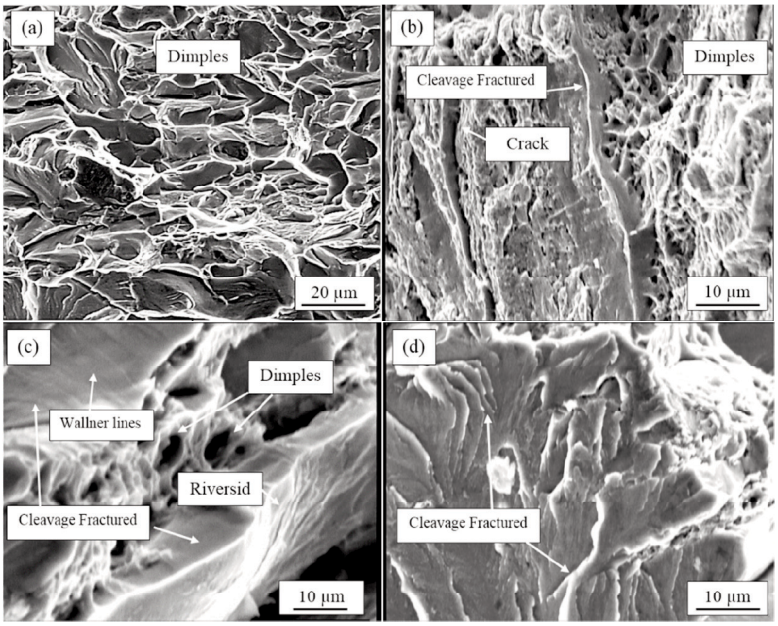

Fig. 6. The SEM fractographs of the (a) sample Bas-rolled, (b) sample $A_{420/120}$, (c) sample $B_{420/120}$ and (d) sample $C_{420/120}$.

seen. Perhaps the most readily recognizable microscopic fracture mechanism is that of intergranular failure wherein the crack prefers to follow the grain interfaces. Also, if the material has an insufficient number of independent slip systems to accommodate plastic deformation between contiguous grains, grain-boundary separation may occur [18]. The cracked boundaries are those of the austenite, which forms at the high-temperature and this austenite transformed to martensite due to its lower stability (in higher Nb content) as confirmed by EBSD results.

The fracture surfaces of the tensile test specimens were subjected to the SEM investigation to understand the failure patterns of Nb-free and Nb microalloyed specimens. The SEM micrographs of the fracture surface of the samples $C_{as\text{-}rolled}$, $A_{420/120}$, $B_{420/120}$ and $C_{420/120}$ can be seen in the Fig. 5. All samples revealed almost different fractography pattern which could be associated to the effect of Nb microalloying element. Because actual fractures rarely occur by pure tension or shear, the various combinations of loading modes I, II, and III, as well as the constant change in orientation of the local plane of fracture as the crack propagates, result in asymmetrical straining of the mating fracture surfaces [18].

The fractured surface of samples $B_{as\text{-}rolled}$ and $A_{420/120}$ consist of the dimples in various sizes and shapes, which means the ductile failure. Depending on the microstructure and plasticity of the material, the dimples can exhibit a very deep and conical shape or can be quite shallow. The dimples are deep and the tearing edges are thick with lots of micropores in Fig. 6(a) in comparison to other samples, while the shallow one also can be seen in Fig. 6(b). The size of the void in the 6(b) specimen is smaller than that in the 6(a) which suggests that a smaller stretch zone was present at the tip of the crack. Moreover, comparing the ductile dimples in Fig. 6(a) and 6(b), it is obvious that the size of ductile dimples became inhomogeneous with applying heat treatment procedure. Thus, it is inferred that the number of ductile dimples was increased and the distribution of ductile dimples became more non-uniform in heat treatment samples, which is due to increase in total elongation. The cleavage fracture also can be seen in Fig. 6(b). This can be attributed to the fracture of harder phases such as stable austenite that transfers to martensite during the deformation and occurrence of TRIP

[DOI: 10.22068/ijmse.15.3.32]

phenomena.

Fig. 6(c) shows two principal fracture modes, dimple rupture and cleavage while the proportion of the cleavage fracture is higher than the dimple one. Sample $B_{420/120}$ is polycrystalline within the soft and hard phases that affect the propagation of the cleavage fracture. These imperfections and changes in the crystal lattice orientation, such as possible mismatch of the low index planes across grain or subgrain boundaries, produce distinct cleavage fracture surface features. The network of cleavage steps is known as a riverside pattern has been shown in this figure [17, 18]. As the fracture advances, the number of active planes decreases by a joining process that forms progressively higher cleavage steps. The crack nuclei are formed at sites where the glide processes are impeded at grain boundaries [17]. Due to the fact that the grains have different orientations with respect to each other, the crack generally divides into terrace-like steps when crossing a grain boundary [18]. The newly created different crack planes join together during further crack propagation producing a characteristic river-like pattern. Wallner lines also are presented in this pattern that constitute a distinct cleavage pattern that is observed on brittle area of the fractured surface. This structure consists of two sets of parallel cleavage steps that often intersect to produce a crisscross pattern [17].

In Fig. 6(d), almost entirely cleavage fracture can be seen in this image which can be attributed to the fracture of primary martensite. The flatness of cleavage facets suggests the idea that only the two atomic planes, which form the fracture surfaces, are involved in the crack process. However, in cleavage, a plastic zone is also formed at the front of a running crack. This plastic zone consumes the main part of the fracture energy. Depending on the lateral extent of the plastic zone, the material near the crack planes is plastically deformed. Facets are typically flat, although they may reflect a parallel plateau and ledge morphology. Often these cleavage steps appear as river patterns wherein fine steps are seen to merge progressively into larger ones. It is generally believed that the flow of the river pattern is in the direction of microscopic crack propagation. Due to the strong differences in the orientations of single martensite blocks, the crossing of the grain boundaries by a crack is hindered analogously to the case of two-phase steel mentioned above, i.e. shear processes must occur to unite the cleavage facets, thus the river pattern is scarcely visible [18].

As revealed through microstructural investigation, the addition of Nb remarkably decrease the bainite transformation due to indirectly accelerate transformation kinetics through grain refinement which is resulting in pro-eutectoid ferrite and upper bainite [6]. Therefore it can be concluded that the dimples are mainly related to fracture of the softer phases such as unstable austenite and α and δ ferrite due to overloading during tensile test. Whilst the cleavage rupture related to the hard phases i.e. primary martensite. Based on the discussion above, it is deduced that the ductility of the sample $A_{420/120}$ is mainly derived from the deformation of ferritic matrix and occurrence of TRIP phenomena as well as the cooperative effect of α and δ-ferrite, bainite, retained austenite, while, the sample $C_{420/120}$ indicates that the presence of primary martensite leading up to cleavage fracture. Thus, by the same conclusion it can be concluded that the excellent mechanical property of sample $A_{420/120}$ is primarily associated with the discontinuous TRIP effect and the cooperative deformation of composite-type structure. Steels with such microstructure feature with characteristics of a composite material, perfectly combining high strength with required plasticity.

CONCLUSIONS

In the present study, Fe-0.4C-3.9Al-1.35Mn (wt.%) TRIP steels with different contents of Nb were subjected to fractography survey. The fracture surfaces of tensile tested specimens were subjected to the SEM investigation to understand the nature failure patterns. The main conclusions of the present study are the followings:

1. The amount of bainite decrease sharply by addition of Nb and the morphology of A/M change from sheaf structure to blocky.
2. The results reveled an unexpected decrease in tensile strength of the specimens by

[DOI: 10.22068/ijmse.15.3.32]

addition of Nb. It should be noted that the sample A420/120 giving rise to the best strength–ductility balance which is the consequence of relatively high volume fraction of retained austenite with high carbon content.

3. The Nb-free and Nb microalloyed samples demonstrated almost different fractography patterns which can be associated to the effect of the Nb microalloying element. The proportion of the cleavage fracture in comparison of dimple rapture increased by increasing the Nb-content due to the increase of primary martensite in the microstructure. It was deduced that the ductility of the sample A420/120 is mainly derived from the deformation of ferritic matrix and occurrence of TRIP phenomena as well as the cooperative effect of α and δ-ferrite, bainite, retained austenite, while for sample C420/120, the presence of primary martensite leading up to cleavage fracture.

ACKNOWLEDGEMENT

We gratefully acknowledge the support from the Iran National Science Foundation [No.:94016117] and Shiraz University.

REFERENCES

1. Cai, Z., "Unique impact of ferrite in influencing austenite stability and deformation behavior in a hot-rolled Fe–Mn–Al–C steel". Materials Science and Engineering: A, 2014, 595, 86-91.
2. Srivastava, A. K., "Effect of heat treatment on microstructure and mechanical properties of cold rolled C–Mn–Si TRIP-aided steel". Materials Characterization, 2006, 57(2), 127-135.
3. Tsuchiyama, T., "Microstructure and mechanical properties of a medium manganese steel treated with interrupted quenching and intercritical annealing". Scripta Materialia, 2016, 122, 36-39.
4. Li, Z., Z. Cai, and R. Misra, "The critical factors governing mechanical properties in hot-rolled Fe-0.2 C-11Mn-(0-6) Al TRIP steels and fracture behavior". Materials Science and Engineering: A, 2017, 683, 46-55.
5. S. Gholami Shiri, S. A. Jenabali Jahromi, Y. Palizdar and M. Belbas, Journal of Iron and Steel Research, International, 2016, 23(9), 988-996.
6. Hausmann, K., "The influence of Nb on transformation behavior and mechanical properties of TRIP-assisted bainitic–ferritic sheet steels". Materials Science and Engineering: A, 2013, 588, 142-150.
7. Song, Y. Y., "Austenite in transformation-induced plasticity steel subjected to multiple isothermal heat treatments". Metallurgical and Materials Transactions A, 2014, 45(10), 4201-4209.
8. A. Grajcar, H. Krztoń. "Effect of isothermal bainitic transformation temperature on retained austenite fraction in C-Mn-Si-Al-Nb-Ti TRIP-type steel. Journal of Achievements in Materials and Manufacturing Engineering", Volume 35 Issue 2 August 2009,169-176.
9. Wei, H., "Hot deformation behavior of two C–Mn–Si based and C–Mn–Al based microalloyed high-strength steels: A comparative study". Materials & Design, 2013, 50, 484-490.
10. Alkan, G., D. Chae, and S. J. Kim, "Effect of δ ferrite on impact property of hot-rolled 12Cr–Ni steel". Materials Science and Engineering: A, 2013, 585, 39-46.
11. Feng, Q., "Microstructures and mechanical properties of hot-rolled Nb-microalloyed TRIP steels by different thermo-mechanical processes". Materials Science and Engineering: A, 2014, 605, 14-21.
12. Dan, W., "The effect of strain-induced martensitic transformation on mechanical properties of TRIP steel". Materials & Design, 2008, 29(3), 604-612.
13. Lacroix, G., T. Pardoen, and P. J. Jacques, "The fracture toughness of TRIP-assisted multiphase steels". Acta Materialia, 2008, 56(15), 3900-3913.
14. Wang, H., "Microstructural evolution and mechanical properties of duplex TRIP steel produced by strip casting". Materials Science and Engineering: A, 2017, 692, 43-52.
15. Zakerinia, H., A. Kermanpur, and A. Najafizadeh, "Color metallography; a suitable method for characterization of martensite and

[DOI: 10.22068/ijmse.15.3.32]

bainite in multiphase steels". International Journal of Iron & Steel Society of Iran, 2009, 6(1), 14-18.
16. E. A. Mertens, "Microstructure and mechanical properties of a mixed Si–Al TRIP-assisted steel subjected to continuous galvanizing heat treatments," Materials Science & Engineering A, 2014, 608, 249-257.
17. R. W. Hertzberg, "Deformation and Fracture Mechanics of Engineering Materials", JOHN WILEY & SONS, INC., New Jersey, USA, 1996, 701-715.
18. ASM Handbook Committee, ASME Handbook, volume 12: fractography, ,United States of America, 1987, 34-140.

[DOI: 10.22068/ijmse.15.3.32]